Insight into Lithium-Ion Mobility in Li2La(TaTi)O7

Journal:	*Journal of Materials Chemistry A*
Manuscript ID	TA-ART-06-2018-005187.R1
Article Type:	Paper
Date Submitted by the Author:	03-Jul-2018
Complete List of Authors:	Fanah, Selorm; University of Louisville Yu, Ming; University of Louisville Huq, Ashfia; Oak Ridge National Laboratory, Neutron Scattering Division Ramezanipour, Fershid; University of Louisville, Chemistry

SCHOLARONE™
Manuscripts

Insight into Lithium-Ion Mobility in $Li_2La(TaTi)O_7$

Selorm Joy Fanah[1], Ming Yu,[2] Ashfia Huq[3], Farshid Ramezanipour[1,]*

[1]Department of Chemistry, University of Louisville, Louisville, KY 40292, USA

[2]Department of Physics and Astronomy, University of Louisville, Louisville, KY 40292, USA

[3]Oak Ridge National Laboratory, Oak Ridge, TN 37931, USA

*Email: farshid.ramezanipour@louisville.edu, Phone: +1(502) 852-7061

ABSTRACT

Combination of neutron diffraction, impedance spectroscopy and DFT analysis of lithium diffusion pathways provides an understanding of lithium-ion mobility in layered oxides through a case study of $Li_2La(TaTi)O_7$. This new material is a Li-conducting oxide, which contains stacks of $(Ta/Ti)O_6$ octahedra separated by a layer of lithium ions, forming the Ruddlesden-Popper type structure. Experiments show that two strategies, i.e., shortening the Li hopping distance and inducing defects in the Li-layer, can successfully improve the ionic conductivity. The DFT analyses reveal the orientation of lithium diffusion pathways and the energy barriers in these pathways, which are directly correlated with the atomic arrangement of this material. These results have broad implications with regard to the design of a new class of Li-conducting oxides based on Ruddlesden-Popper oxides.

INTRODUCTION

The need for development of solid lithium-ion conductors has been recognized in recent years,[1-5] and there has been intense research on development of solid electrolytes for lithium ion batteries. Several classes of solids have been investigated for this purpose, including different polymers,[6, 7] perovskite[8, 9] and garnet oxides.[1-3, 10] Another family of oxides that has the potential to be a good lithium-ion conductor is the Ruddlesden-Popper family. This class of oxides has been studied in view of various properties they exhibit such as ion-exchange,[11] carbon dioxide (CO_2) capture,[12] and photocatalytic activities.[13] However, little work has been done on their potential Li-ion conductivity. Solid electrolytes need to have structures and compositions that allow the conduction of lithium ions, but have negligible electronic conductivity. While it is possible to incorporate Li-ions in a diverse range of solid-state compounds, the conduction pathways that allow the mobility of lithium ions are not available in many lithium-containing compounds. However, Ruddlesden-Popper materials have open spaces in their structure that can be ideal pathways for lithium-ion conductivity. In addition, the diverse range of possible compositions makes it possible to design Li-containing Ruddlesden-Popper compounds that have negligible electronic conductivity. As shown in Figure 1, the structure of these materials comprises layers of corner-sharing BO_6 octahedra, where B is usually a transition metal. These layers are stacked to form double or triple layer slabs. The general formula for these oxides is $A_{n+1}B_nO_{3n+1}$, where A is usually an alkaline-earth or lanthanide cation located in spaces within and between the octahedral stacks. The number of layers in each stack in represented by n = 1, 2 or 3. Given the large gap between the stacks, it is reasonable to speculate that the inter-stack spaces could be good pathways for transport of ions. If lithium-containing Ruddlesden-Popper compounds can be synthesized, it should be possible to achieve Li-ion conductivity. A small number of n = 2

Ruddlesden-Popper oxides containing lithium have been reported, [12, 14-16] where the Li ions reside in spaces between the stacks. The electrical conductivity of a composite system, containing poly(ethylene oxide) and Ruddlesden-Popper compounds, has been investigated recently, suggesting a two-dimensional Li-conduction pathway based on bond valence sum mapping.[17] Also, the electrical properties of $Li_2SrTa_2O_7$ has been studied, showing lithium-ion conductivity.[18] It has been suggested that creating partial cation deficiency in the intra-stack sites can lead to the displacement of some lithium ions at elevated temperatures form inter-stack to intra-stack positions, leaving behind vacant sites.[18] While the ionic conductivity of $Li_2SrTa_2O_7$ is not significant, it demonstrates the feasibility of lithium conduction in Ruddlesden–Popper phases. This is reminiscent of the initial stages of research on some other ionic conductors, such as garnet oxides, where the first materials showed low lithium ion mobility,[4] but further modifications led to the synthesis of highly conductive materials.[1-3, 10]

Further optimization of Ruddlesden-Popper compounds can lead to enhanced lithium ion conductivity. Given the presence of large cations, such as Sr^{2+}, in $Li_2SrTa_2O_7$, we hypothesized that the ionic conductivity should be enhanced if the synthesis of Ruddlesden-Popper compounds containing smaller cations on both A and B-sites could be achieved. Cations that have smaller ionic radii will lead to smaller unit cells, shortening the hopping distances for lithium ions. Therefore, we planned to synthesize $Li_2La(TaTi)O_7$, containing La^{3+} and Ti^{4+}, which have smaller ionic radii than Sr^{2+} and Ta^{5+}, respectively. In addition, we sought to enhance the ionic conductivity further by inducing defects directly in the Li-layer to improve the mobility of lithium ions. This paper describes the results of these studies. While the lithium ion conductivity still needs to be improved for practical applications, this work demonstrates the success of the above strategies for enhancing the ionic conductivity in Ruddlesden-Popper oxides.

EXPERIMENTAL AND COMPUTATIONAL METHODS

Synthesis: The syntheses were performed by solid-state method using powders of Li_2CO_3 (Alfa Aeasar, 99.998%), La_2O_3 (Alfa Aeasar, 99.99%), Ta_2O_5 (Alfa Aeasar, 99.993%), and TiO_2 (Sigma Aldrich, 99.99%). Stoichiometric amounts of precursors were weighed and mixed together. In order to compensate for Li loss due to evaporation at high temperature, 5% extra Li_2CO_3 was added to the starting mixture. The mixtures were then ground and pressed into pellets and calcined in alumina crucibles at 850 ºC for 4 hours. The calcined pellets were ground, re-pelletized and re-fired at 1200 ºC for 6 hours in air. The heating and cooling rates in all cases were 100 °C/hour. Both $Li_2La(TaTi)O_7$ and the A-site deficient $Li_{1.8}La(Ta_{1.2}Ti_{0.8})O_7$ were synthesized as single phase products. Attempts to create further A-site deficiency, beyond 0.2 moles per formula unit, led to impure products.

Characterization: The polycrystalline oxides were studied by Powder X-ray diffraction (PXRD) using Cu $K\alpha_1$ radiation (λ= 1.54056 Å) in 2θ range 5 – 100º. The crystal structures of all samples were examined by Rietveld refinements using GSAS software,[19] and EXPGUI interface.[20]

Microstructural characterization was perfumed using high-resolution field-emission scanning electron microscopy (SEM).

Neutron diffraction experiments were performed on POWGEN diffractometer at Spallation Neutron Source in Oak Ridge National Laboratory at 300 K, over the d-range of 0.25 – 5 Å.

Ionic conductivity measurements on sintered pellets (~1.45 mm in thickness and 9 mm in diameter) were carried out using a computer controlled potentiostat equipped with a frequency response analyzer in the frequency range 0.1 Hz to 1 MHz and temperature range 25 to 400 ºC in

air. All conductivity measurements were performed under identical conditions for both the parent compound and the A-site deficient analogue.

Density Functional Theory Calculations: The overall computational calculations were mainly carried out employing the density functional theory (DFT)[21, 22] framework, as implemented in the Vienna Ab-initio Simulation Package (VASP).[23] The electron-ion interactions were described by the Projector Augmented Wave (PAW)[24], while electron exchange-correlation interactions were treated by the generalized gradient approximation (GGA)[25] in the scheme of Perdew Burke Ernzerhof (PBE).[26] The spin polarized behaviors were also considered in calculations. The structural relaxation was performed using Congregate-Gradient algorithm[27] implemented in VASP. The micro-canonical ensemble was used in the Molecular Dynamics simulation and all atoms in the unit cell were allowed to move freely during the simulations. An energy cutoff was set at 400 eV for the plane wave basis in all calculations, and the criteria for convergences of energy and force in relaxation processes were set to be 10^{-5} eV and 10^{-4} eV/Å, respectively. A 1x1x1 primitive cell was chosen and the Brillouin zones (BZ) were sampled by $5 \times 5 \times 5$ k-point meshes generated in accordance with the Monkhorst-Pack scheme[28] in all calculations.

RESULTS AND DISCUSSIONS

Crystal Structure

Both $Li_2La(TaTi)O_7$ and $Li_{1.8}La(Ta_{1.2}Ti_{0.8})O_7$ have double-layered Ruddlesden-Popper structure type, $A_{n+1}B_nO_{3n+1}$, where n = 2. The double-layered Ruddlesden-Popper materials usually have tetragonal[14, 29, 30] or orthorhombic[15, 16, 31] structures. The common space groups are I4/mmm,[14, 29] $P4_2$/mmm,[30] Fmmm[15, 32] and Cmcm.[16, 31]

For $Li_2La(TaTi)O_7$, the tetragonal structure is readily ruled out due to the splitting of the X-ray diffraction peaks at 2θ = 58.8, 68.0, 77.4, 81.5, 92.8, and 96.1°, indicating that this material crystalizes in an orthorhombic space group. Given the angle-dependence of the peak intensities in X-ray diffraction, the peaks at high 2θ angle (low d-spacing) are not pronounced. However, this problem does not exist in neutron diffraction, which allows for careful examination of the peaks in low d region. The neutron diffraction data show small peaks at d = 1.115 Å and 1.505 Å, which cannot be described by *Fmmm* space group, but are an excellent match with *Cmcm*. Figures 2 and 3 show the refinement profile for $Li_2La(TaTi)O_7$ using *Cmcm* model with both X-ray and neutron diffraction data, respectively.

The accurate determination of oxygen and lithium positions in $Li_2La(TaTi)O_7$ was performed using neutron diffraction. The limitations of laboratory powder X-ray diffraciton in the study of light atoms such as lithium and oxygen should be noted. These limitaitons can lead to the observaiton of unrealistic distortions in the coordination environment of lithium. However, neutron diffraciton can reaidly identify and study these light atoms. Table 1 lists the refined structural parameters for $Li_2La(TaTi)O_7$.

Interestingly, the A-site deficiency leads to a change in space group of $Li_2La(TaTi)O_7$. The A-site deficient compound, $Li_{1.8}La(Ta_{1.2}Ti_{0.8})O_7$, does not show the orthorhombic peak splitting discussed above. This material has a tetragonal structure, with space group *I4/mmm*, as shown in Figure 2. The insets in this figure highlight the difference between the powder diffraction data for $Li_2La(TaTi)O_7$ and the A-site deficient $Li_{1.8}La(Ta_{1.2}Ti_{0.8})O_7$. The refined structural parameters for $Li_{1.8}La(Ta_{1.2}Ti_{0.8})O_7$ are listed in Table 2.

In both parent and the A-site deficient compounds, the $(Ta/Ti)O_6$ octahedra form double-layer stacks by corner-sharing. The octahedra are distorted in both compounds. The La atoms are

located in spaces within the stacks, while Li atoms reside in inter-stack spaces, as shown in Figure 1. The Li atoms have distorted tetrahedral coordination geometry and form a layer of edge-sharing tetrahedra between the octahedral stacks. As described later, the ionic conducitivty occurs through this lithium layer.

The scanning electrom microscopy data in Figure 4 show that the microstucture of $Li_2La(TaTi)O_7$ remains nearly unaffected due to A-site deficency. However, the ionic conducitvty improves signifcantly, as discussed below.

Lithium-Ion Conductivity

Variable temperature electrochemical impedance spectroscopy shows an increase in ionic conductivity as a function of temperature, as listed in Table 3. The impedance plots of $Li_2La(TaTi)O_7$ in the Nyquist plane in the temperature range 100 – 400 °C are presented in Figure 5. The observed spike (tail) in the low-frequency region indicates the blocking of mobile lithium ions at the electrodes.[9, 18, 33-35] The appearance of a semicircle in the high-frequency region was observed only at temperatures above 100 ºC. There was no semicircle and measurable conductivity at room temperature, which can be due to the restriction of lithium ion mobility, since all lithium sites between the layers are occupied, as seen from the crystal structure in Figure 1. A similar behavior, i.e., lack of room temperature conductivity, was reported for the layered perovskite $Li_2Sr_{1.5}Nb_3O_{10}$, even though some defects had been introduced in the crystal structure. [36] We will show later that, for $Li_2La(TaTi)O_7$, lack of ionic conductivity at room temperature can be overcome by introducing vacancies in some lithium sites. The increase in

conductivity with temperature is expected due to an increase in mobility of ions and a decrease in grain boundary resistance.[37,34]

The total conductivity (grain and grain boundary) of $Li_2La(TaTi)O_7$ was determined from the intercept with real axis in the low frequency region of the Nyquist plot. Figure 6 shows a typical fit for the Nyquist plot at 200 °C. Fitting of the semicircle with only one resistance-capacitance (RC) element is not possible. This is due to the merging of two relaxation processes, occurring at similar time scales.[30] The two processes correspond to contributions from bulk and grain boundary. To estimate these contributions, we built an electrical model as seen in the inset of Figure 6.[30] Then first RC unit (R1= 1.71×10^5 Ω and CPE1=5.9×10^{-11} F) correspond to the bulk (grain), and the second set (R2= 1.2×10^6 Ω and CPE2=3.0×10^{-10} F) correspond to the grain boundary. As expected, the respective capacitance values for bulk, grain boundary and electrode (CPE3) are in the order of 10^{-11}, 10^{-10} and 10^{-7} F, respectively.[9, 33, 38] The same model can be used for fitting at 300 °C, leading to smaller resistances (R) for both bulk, 26700 Ω, and grain boundary, 39426 Ω, compared to the resistances at 200 °C, which were discussed above.

The importance of composition design is demostrated when $Li_2La(TaTi)O_7$ is compared to another compound with the same structure-type, $Li_2SrTa_2O_7$.[18] The conductivity of $Li_2SrTa_2O_7$ has been reported at 300 °C. At this temperature, $Li_2SrTa_2O_7$ shows conductivity of 5.0×10^{-7} Scm^{-1}. However, at the same temperature, the conductivity value for $Li_2La(TaTi)O_7$ is 3.5×10^{-6} S cm^{-1}, one order of magnitude greater than that of $Li_2SrTa_2O_7$. The enhanced conductivity of $Li_2La(TaTi)O_7$ can be due to the smaller ionic radii of the A-site and B-site cations in this material's composition, leading to shorter hopping distances for Li^+. The distance between two neighboring Li-sites is as short as ~2.75 Å, while the same distance for $Li_2SrTa_2O_7$ is ~2.80 Å.[18] This indicates the success of our strategy in designing $Li_2La(TaTi)O_7$ composition.

8

We also examined the effect of creating vacant sites in the Li layer by synthesizing $Li_{1.8}La(Ta_{1.2}Ti_{0.8})O_7$. This was done in an attempt to allow lithium ions to move more freely in the inter-stack spaces. In this material, 10% Li vacancies were introduced and charge neutrality was maintained by changing the Ta/Ti ratio from 1/1 to 1.2/0.8. This lithium deficient compound showed significantly enhanced ionic conductivity compared to the parent $Li_2La(TaTi)O_7$. The conductivity values, derived from the intercept with real axis in the low frequency region of the Nyquist plot, are listed in Table 3. As seen here, the conductivity of the Li-deficient compound is one to two orders of magnitude greater than that of $Li_2La(TaTi)O_7$ at different temperatures, reaching 1.08×10^{-3} S cm^{-1} at 400 ºC. Note that the Li-deficient compound shows measurable conductivity and a semicircle in Nyquist plot even at room temperature, as shown in Figure 7. This semicircle, at both 25 °C and 100 °C, could be described by three RC elements (Figure 8), similar to some other ionic conductors such as lithium lanthanum titanate perovskite,[9, 38] where the third RC element has been assigned to electrode interface.[38] This electrode RC unit has resistance and capacitance values, $R3 = 1.23 \times 10^7$ Ω and $CPE3 = 1.40 \times 10^{-7}$ F, respectively. The first ($R1 = 1.15 \times 10^6$ Ω and $CPE1 = 5.099 \times 10^{-11}$ F) and second ($R2 = 5.37 \times 10^5$ Ω and $CPE2 = 6.53 \times 10^{-10}$ F) RC elements correspond to bulk and grain boundary, respectively. As expected, all three resistance contributions at 100 °C are smaller than those at 25 °C, where the bulk, grain boundry and electrode interface resistances are 4.33×10^6, 2.19×10^7 and 4.10×10^7 Ω, respectively. As seen in Figures 5 and 7, for both compounds, the semicircles gradually shrink with increase in temperature and the contributions from bulk and grain boundary can not be separated beyond 300 °C for the parent compound and above 100 °C for the Li-deficient material. The disappearance of semicircles with increase in temperature is commonly observed in ionic conductors such as garnets.[35, 37, 39, 40]

As shown in Table 3, the conductivity of the Li-deficient compound increases significantly above room temperature, rising from 4.08×10^{-9} to 1.08×10^{-3} S cm^{-1} at 400 ℃. The activation energy for the rise in conductivity as a function of temperature can be obtained using the Arrhenius equation for thermally activated conductivity:[41-43]

$$\sigma T = \sigma_o e^{-Ea/kT}$$

where σ_o is the pre-exponential factor, characteristic of the material and E_a, k and T are the activation energy, Boltzmann constant, and the absolute temperature, respectively. The Arrhenius plots for electrical conductivity of both $Li_2La(TaTi)O_7$ and the Li-deficient $Li_{1.8}La(Ta_{1.2}Ti_{0.8})O_7$ are shown in Figure 9. The activation energy (E_a) decreases when vacancies are introduced in the lithium layers. Activation energies are 0.61 eV and 0.57 eV for $Li_2La(TaTi)O_7$ and $Li_{1.8}La(Ta_{1.2}Ti_{0.8})O_7$, respectively.

The differences between the ionic conductivity of the A-site deficient and parent compound, and the large increase in conductivity due to A-site vacancies, indicate that the pathway for lithium ion conduction is through the inter-stack layer. As discussed below, the lithium conduction pathway is confirmed by computational study.

Density Functional Theory Calculations

To study the lithium ion diffusion, a DFT optimized structure was needed. Therefore, the $Li_2La(TaTi)O_7$ crystal structure was optimized. Various configurations with different Ta/Ti distributions were considered. The crystalline structure for each configuration was fully relaxed and the lattice constants corresponding to each configuration were optimized. The optimized structures and the total energies corresponding to each configuration are shown in Figure 10. It

was found that the optimized lattice constants for various configurations were the same, and within 1% of the values obtained using neutron diffraction experiments, indicating an excellent match. From comparing the total energies for different distributions of Ta and Ti, it was found that several configurations had similar energies, but among them the first configuration in Figure 10 was the most favorable. This optimized structure was used for electronic density of states (DOS), electronic band structure, and Li-diffusion studies. In this configuration all Ta and Ti atoms are alternately distributed within the layers and between layers, such that identical metal atoms are separated from each other. A truly randomized distribution of Ta and Ti, similar to that determined from neutron diffraction, would require performing the calculations over hundreds or even thousands of unit cells, which is impractical.

The DOS and band structure of the optimized $Li_2La(TaTi)O_7$ configuration are shown in Figure 11, the system shows a large band gap of 2.0276 eV.

To study the degree of Li mobility in the optimized $Li_2LaTaTiO_7$ structure, the diffusion energy barrier was calculated along b- and c-axes directions, as shown in Figure 12. The diffusion energy barrier is defined as the relative energy at a particular site along the diffusion pathway with respect to the energy at the initial position. The corresponding energy barriers for displacement of lithium by different distances from the original lithium position are shown in Figure 12. The energy barriers along both b and c directions overlap and show the same trend, indicating an isotropic Li diffusion between layers. The two peaks in Figure 12 indicate the high energy barriers, where the distances between Li and O atoms become as short as ~ 1.64 Å (see insets in Figure 12). The energy barrier of ~ 1 eV is high compared to some other ionic conductors.[44, 45] For example, the Li diffusion in phosphorene have energy barrier of ~ 0.1 eV,[46] significantly smaller that the value for $Li_2La(TaTi)O_7$.

The diagonal Li diffusion in the *bc* plane was also investigated, leading to huge energy barriers, in the order of 38 eV. Therefore, it is clear that lithium ions can not diffuse in diagonal direction. The diffusion pathway is therefore along the *b* and *c* directions. The main barrier to the Li diffusion along these pathways is the proximity of Li to O atoms at some positions along the conduction pathway. These results reveal that such short distances in inter-stack spaces should be eliminated in order to design structures with enhanced Li mobility. One way to achieve this goal can be the incorporation of a small amount of a large cation, such as Sr^{2+} or La^{3+}, in inter-layer spaces, which can push the layers apart and open more space between them. Although, this will lead to slightly lower Li concentration in inter-layer spaces, the formation of wider channels can prevent close interactions between Li and O atoms, and can increase Li-ion conductivity.

CONCLUSIONS

The study of lithium-ion mobility in $Li_2La(TaTi)O_7$ and its A-site deficient analogue shows the potential of Ruddlesden-Popper oxides for Li-ion conductivity. The enhanced ionic conductivity of $Li_2La(TaTi)O_7$ and further improvement due to the A-site deficiency indicate the success of two strategies: (a) Designing compositions where Li hopping distances are shortened. (b) Creating defects in the lithium layer to enhance the mobility of lithium ions. The latter also indicates that lithium-ion conductivity pathway is within the inter-stack spaces. This is confirmed by DFT calculations which show the direction of the pathways for lithium mobility and determine the energy barriers for each conduction pathway. These findings can be used for future research to design Ruddlesden-Popper oxides with enhanced lithium-ion conductivity.

ACKNOWLEDGEMENTS

CONFLICT OF INTEREST

The authors declare no conflict of interest.

References:

1. S. Narayanan, F. Ramezanipour and V. Thangadurai, *Inorganic Chemistry*, 2015, **54**, 6968-6977.

2. S. Narayanan, F. Ramezanipour and V. Thangadurai, *The Journal of Physical Chemistry C*, 2012, **116**, 20154-20162.

3. A. K. Baral, S. Narayanan, F. Ramezanipour and V. Thangadurai, *Physical Chemistry Chemical Physics*, 2014, **16**, 11356-11365.

4. V. Thangadurai, H. Kaack and W. Weppner, *Journal of American Ceramic Society*, 2003, **86**, 437-440.

5. B. Scrosati and J. Garche, *Journal of Power Sources*, 2010, **195**, 2419-2430.

6. H. Meyer Wolfgang, *Advanced Materials*, 1999, **10**, 439-448.

7. L. Long, S. Wang, M. Xiao and Y. Meng, *Journal of Materials Chemistry A*, 2016, **4**, 10038-10069.

8. Y. Inaguma, T. Katsumata, M. Itoh and Y. Morii, *Journal of Solid State Chemistry*, 2002, **166**, 67-72.

9. J.-F. Wu and X. Guo, *Solid State Ionics*, 2017, **310**, 38-43.

10. Y. Li, C.-A. Wang, H. Xie, J. Cheng and J. B. Goodenough, *Electrochemistry Communications*, 2011, **13**, 1289-1292.

11. J. Gopalakrishnan and V. Bhat, *Inorganic Chemistry*, 1987, **26**, 4299-4301.

12. C. Galven, J. L. Fourquet, E. Suard, M. P. Crosnier-Lopez and F. Le Berre, *Dalton Trans*, 2010, **39**, 4191-4197.

13. K. Domen, J. S. T. Yoshimura, A. Tanaka and T. Onishi, *Catalytic Lettered*, 1990, **4**, 339.

14.	N. S. P. Bhuvanesh, M.-P. Crosnier-Lopez, H. Duroy and J.-L. Fourquet, *Journal of Materials Chemistry*, 2000, **10**, 1685-1692.

15.	Z. Liang, K. Tang, Q. Shao, G. Li, S. Zeng and H. Zheng, *Journal of Solid State Chemistry*, 2008, **181**, 964-970.

16.	T. Pagnier, N. Rosman, C. Galven, E. Suard, J. L. Fourquet, F. Le Berre and M. P. Crosnier-Lopez, *Journal of Solid State Chemistry*, 2009, **182**, 317-326.

17.	P. Ramakrishnan, H. Kwak, Y.-H. Cho and H. Kim Jae, *ChemElectroChem*, 2018, **5**, 1265-1271.

18.	T. Fukushima, S. Suzuki and M. Miyayama, *Key Engineering Materials*, 2009, **388**, 69-72.

19.	A. C. Larson and R. B. Von Dreele, *General Structure Analysis System (GSAS), Los Alamos National Laboratory Report LAUR* 2004, 86–748.

20.	B. Toby, *Journal of Applied Crystallography*, 2001, **34**, 210-213.

21.	P. Hohenberg and W. Kohn, *Physical Review*, 1964, **136**, B864-B871.

22.	W. Kohn and L. J. Sham, *Physical Review*, 1965, **140**, A1133-A1138.

23.	G. Kresse and J. Furthmüller, *Physical Review B*, 1996, **54**, 11169-11186.

24.	P. E. Blöchl, *Physical Review B*, 1994, **50**, 17953-17979.

25.	J. P. Perdew, J. A. Chevary, S. H. Vosko, K. A. Jackson, M. R. Pederson, D. J. Singh and C. Fiolhais, *Physical Review B*, 1992, **46**, 6671-6687.

26.	J. P. Perdew, K. Burke and M. Ernzerhof, *Physical Review Letters*, 1996, **77**, 3865-3868.

27.	X. Gonze, *Physical Review B*, 1997, **55**, 10337-10354.

28.	H. J. Monkhorst and J. D. Pack, *Physical Review B*, 1976, **13**, 5188-5192.

29.	M.-P. Crosnier-Lopez, F. Le Berre and J.-L. Fourquet, *Journal of Materials Chemistry*, 2001, **11**, 1146-1151.

30.	F. Le Berre, M.-P. Crosnier-Lopez, Y. Laligant, E. Suard, O. Bohnke, J. Emery and J.-L. Fourquet, *Journal of Materials Chemistry*, 2004, **14**, 3558-3565.

31.	S. K. Singh and V. R. K. Murthy, *Materials Research Bulletin*, 2015, **70**, 514-518.

32.	N. S. P. Bhuvanesh, M. P. Crosnier-Lopez, H. Duroy and J. L. Fourquet, *Journal of Materials Chemistry*, 1999, **9**, 3093-3100.

33.	J. Irvine, D. Sinclair and A. West, *Advanced Materials*, 1990, **2**, 132-138.

34.   R. Murugan, W. Weppner, P. Schmid-Beurmann and V. Thangadurai, *Materials Research Bulletin*, 2008, **43**, 2579-2591.

35.   V. Thangadurai and W. Weppner, *Advanced Functional Materials*, 2005, **15**, 107-112.

36.   N. S. P. Bhuvanesh, M. P. Crosnier-Lopez, O. Bohnke, J. Emery and J. L. Fourquet, *Chem. Mater*, 1999, **11**, 634-641.

37.   V. Thangadurai and W. Weppner, *Journal of the American Ceramic Society*, 2005, **88**, 411-418.

38.   O. Bohnke, J. Emery and J.-L. Fourquet, *Solid State Ionics*, 2003, **158**, 119-132.

39.   V. Thangadurai and W. Weppner, *Journal of Solid State Chemistry*, 2006, **179**, 974-984.

40.   V. Thangadurai and W. Weppner, *Ionics*, 2006, **12**, 81-92.

41.   E. Asenath-Smith, I. N. Lokuhewa, S. T. Misture and D. D. Edwards, *Journal of Solid State Chemistry*, 2010, **183**, 1670-1677.

42.   R. Andoulsi, K. Horchani-naifer and M. Férid, *Ceramics International*, 2013, **39**, 6527–6531.

43.   S. Pizzini, *Physical Chemistry of Semiconductor Materials and Processes*, John Wiley & Sons Ltd., West Sussex, U.K., 2015.

44.   H. Wang, Y. Chen, D. Hood Zachary, G. Sahu, S. Pandian Amaresh, K. Keum Jong, K. An and C. Liang, *Angewandte Chemie International Edition*, 2016, **55**, 8551-8555.

45.   I.-H. Chu, C. S. Kompella, H. Nguyen, Z. Zhu, S. Hy, Z. Deng, Y. S. Meng and S. P. Ong, *Scientific Reports*, 2016, **6**, 33733.

46.   Z. Congyan, Y. Ming, A. George, D. Ruchira Ravinath and S. Gamini, *Nanotechnology*, 2017, **28**, 075401.
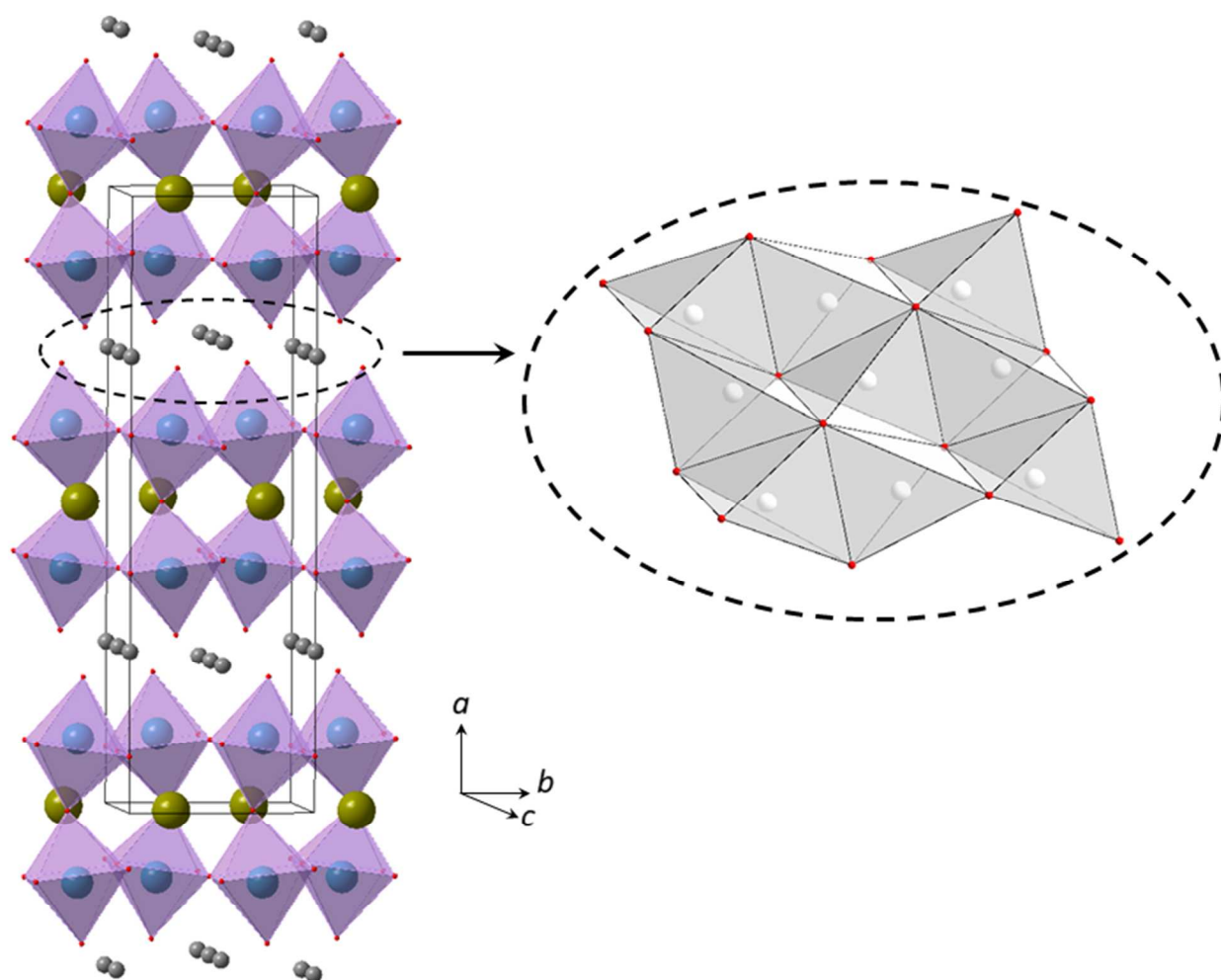
Figure 1. Crystal structure of Li$_2$La(TaTi)O$_7$ (left) and the tetrahedral coordinaiton of lithium atoms (right). Green, blue, gray and red spehres show La, Ta/Ti, Li, and O, respecively.

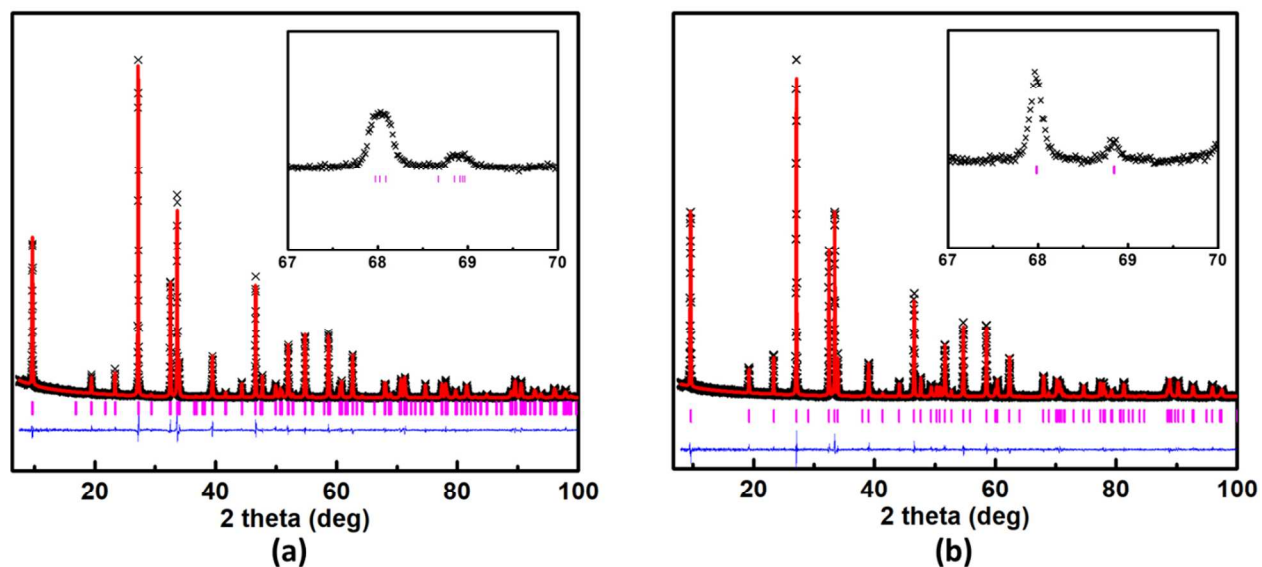**Figure 2.** Rietveld refinement profile for powder X-ray diffraction data (a) $Li_2La(TaTi)O_7$ in *Cmcm* space group. (b) $Li_{1.8}La(Ta_{1.2}Ti_{0.8})O_7$ in *I4/mmm* space group. The black crosses represent experimnatl data, red line shows the fit, vertical tick marks show Bragg peak positions, green horizontal line shows the background fit, and the lower blue line is the diffrence plot.
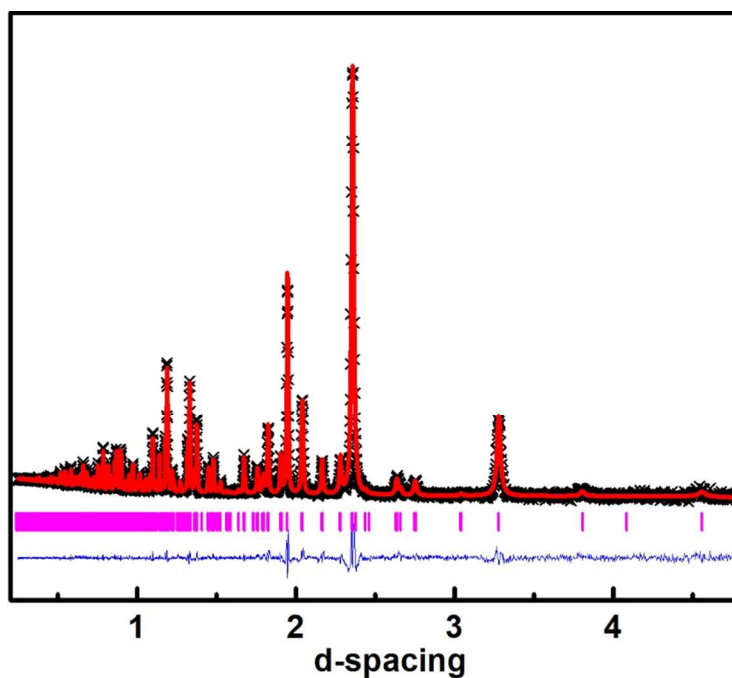
Figure 3. Neutron diffraction Rietveld refinement profile for $Li_2La(TaTi)O_7$ in Cmcm space group.
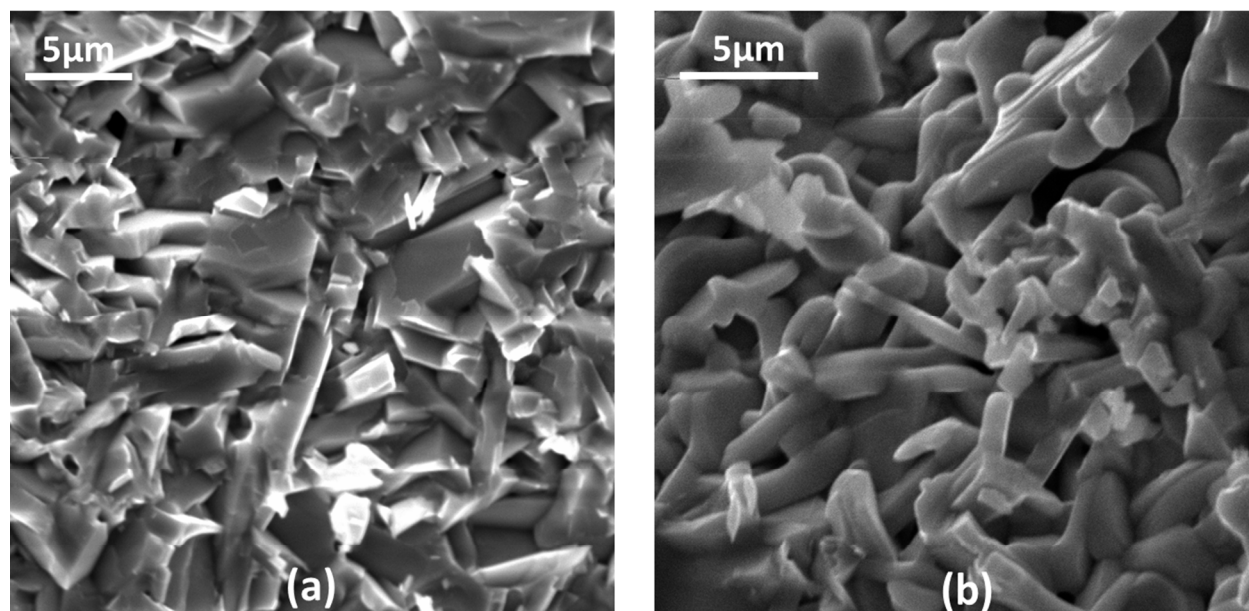
Figure 4. Scanning electron microscopy data for (a) $Li_2La(TaTi)O_7$ and (b) $Li_{1.8}La(Ta_{1.2}Ti_{0.8})O_7$.
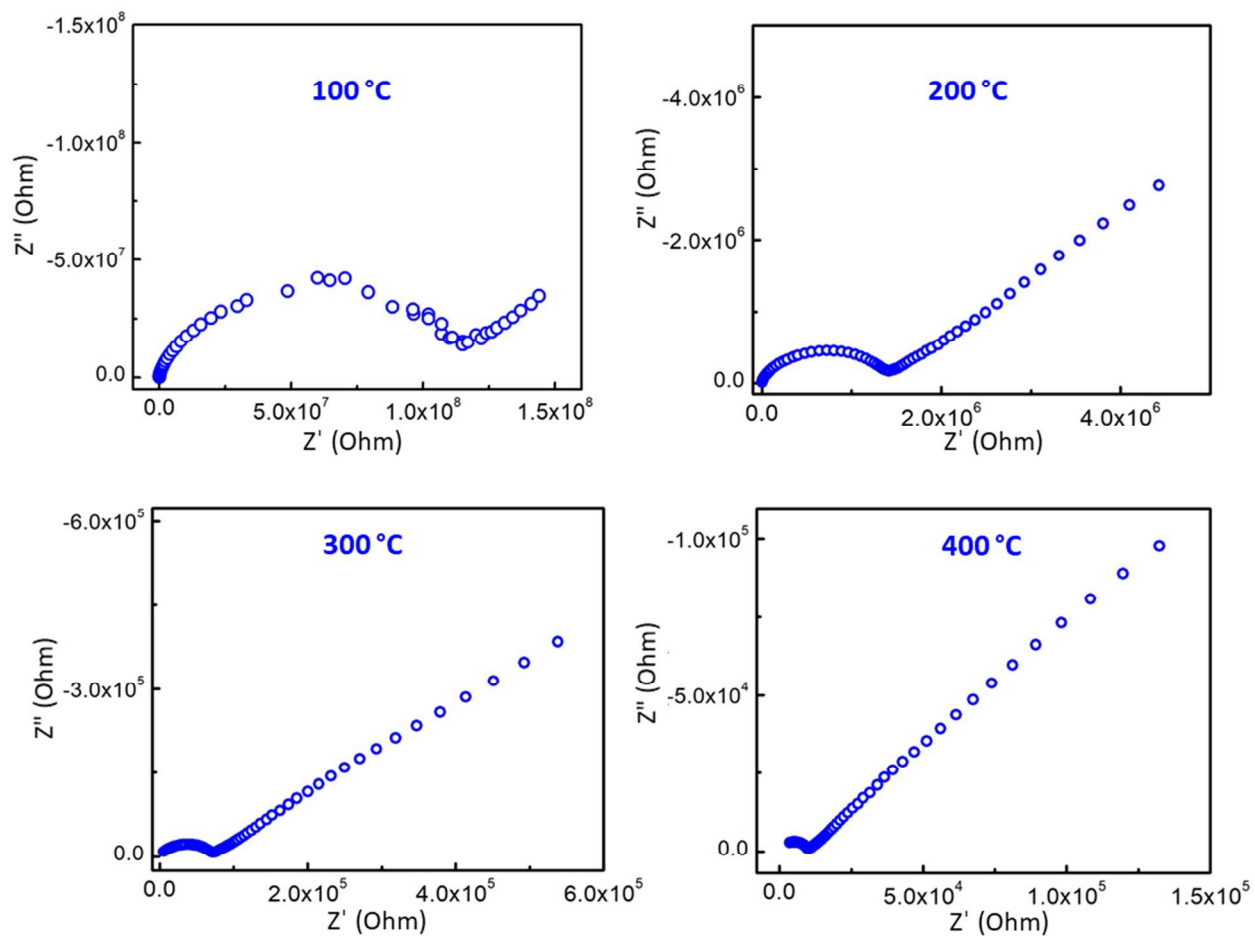
Figure 5. Nyquist Impedance plots for $Li_2La(TaTi)O_7$
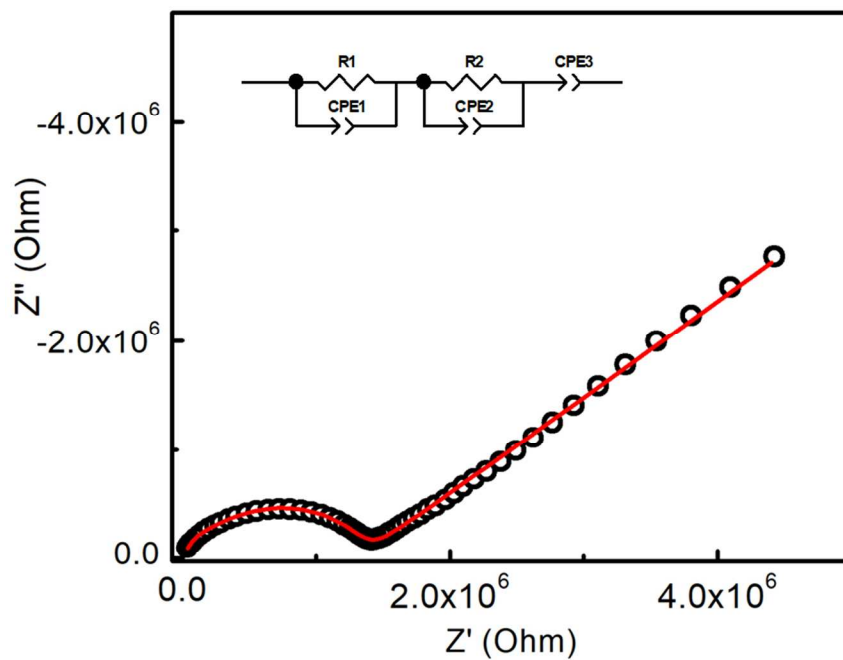
Figure 6. Typical fit to Nyquist Impedance plot for $Li_2La(TaTi)O_7$ at 200 °C.
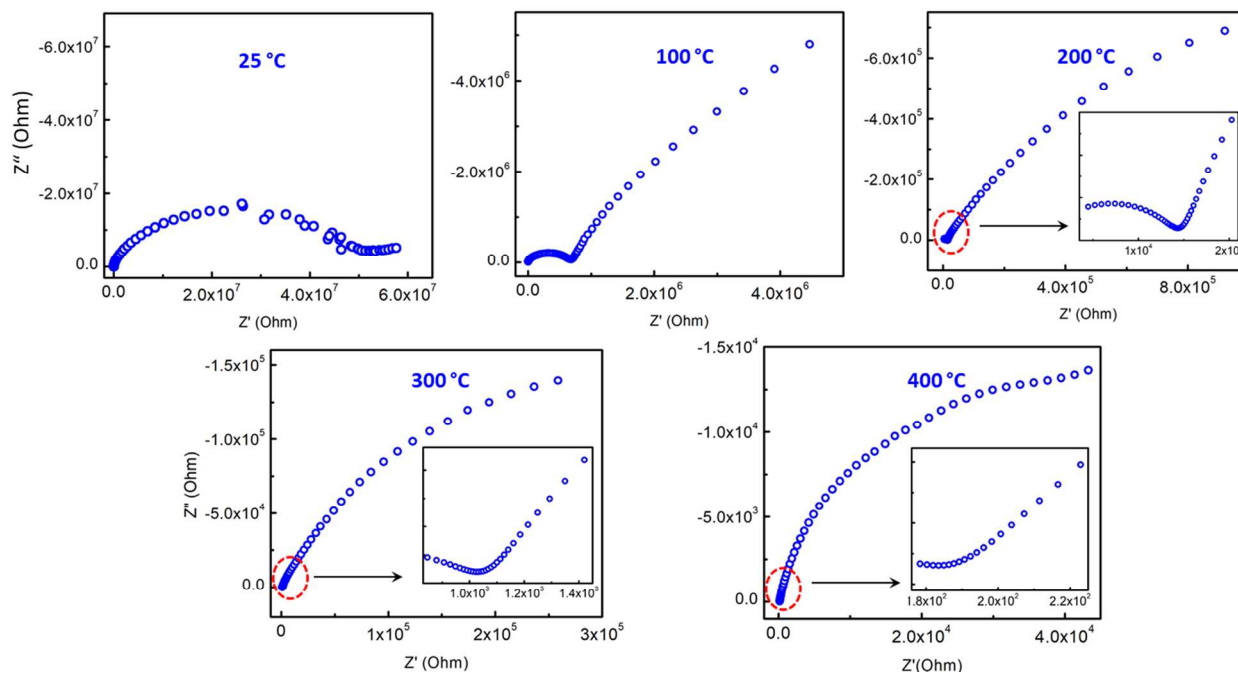
Figure 7. Nyquist Impedance plots for $Li_{1.8}La(Ta_{1.2}Ti_{0.8})O_7$.
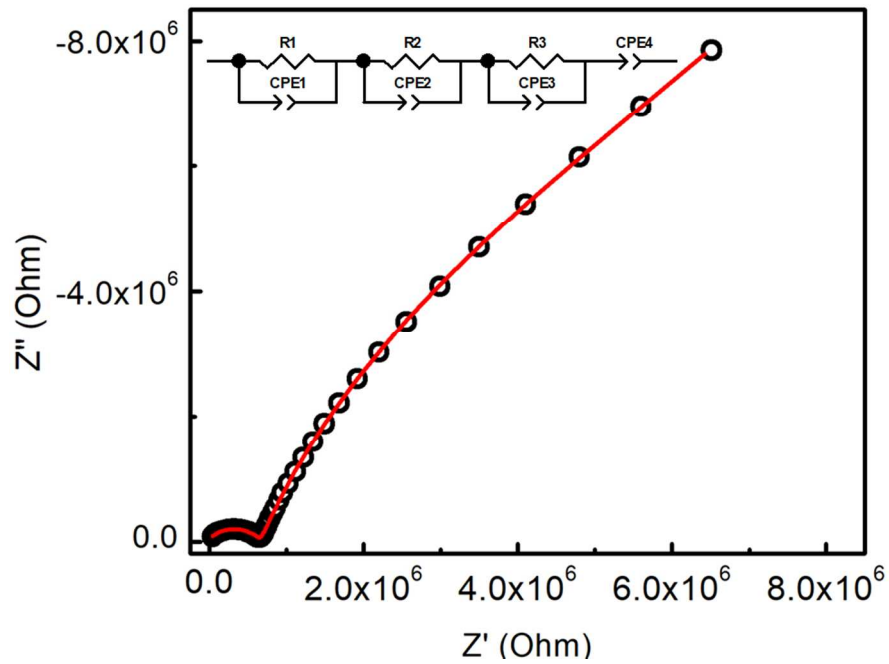
Figure 8. Typical fit to Nyquist Impedance plot for $Li_{1.8}La(Ta_{1.2}Ti_{0.8})O_7$ at 100 °C.
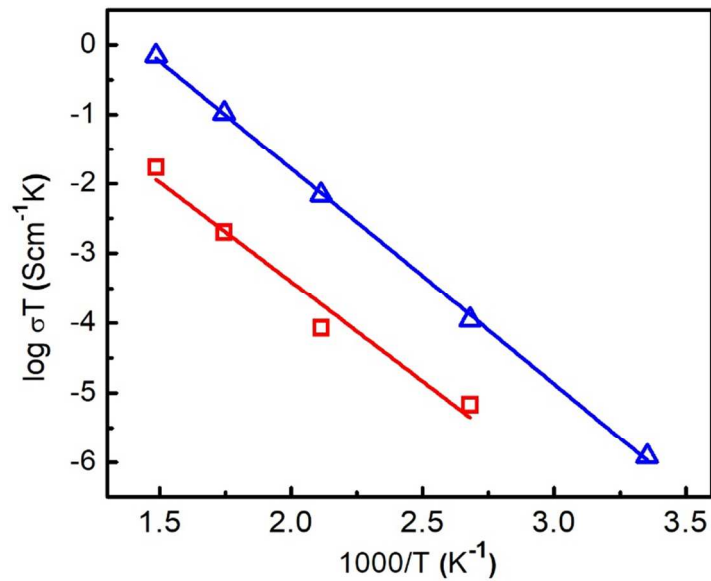
Figure 9. Arrhenius plots for $Li_2La(TaTi)O_7$ (red) and $Li_{1.8}La(Ta_{1.2}Ti_{0.8})O_7$ (blue).

-391.94889 eV   -391.8712 eV   -391.9105 eV   -391.8708 eV   -391.46589 eV   -391.46552 eV

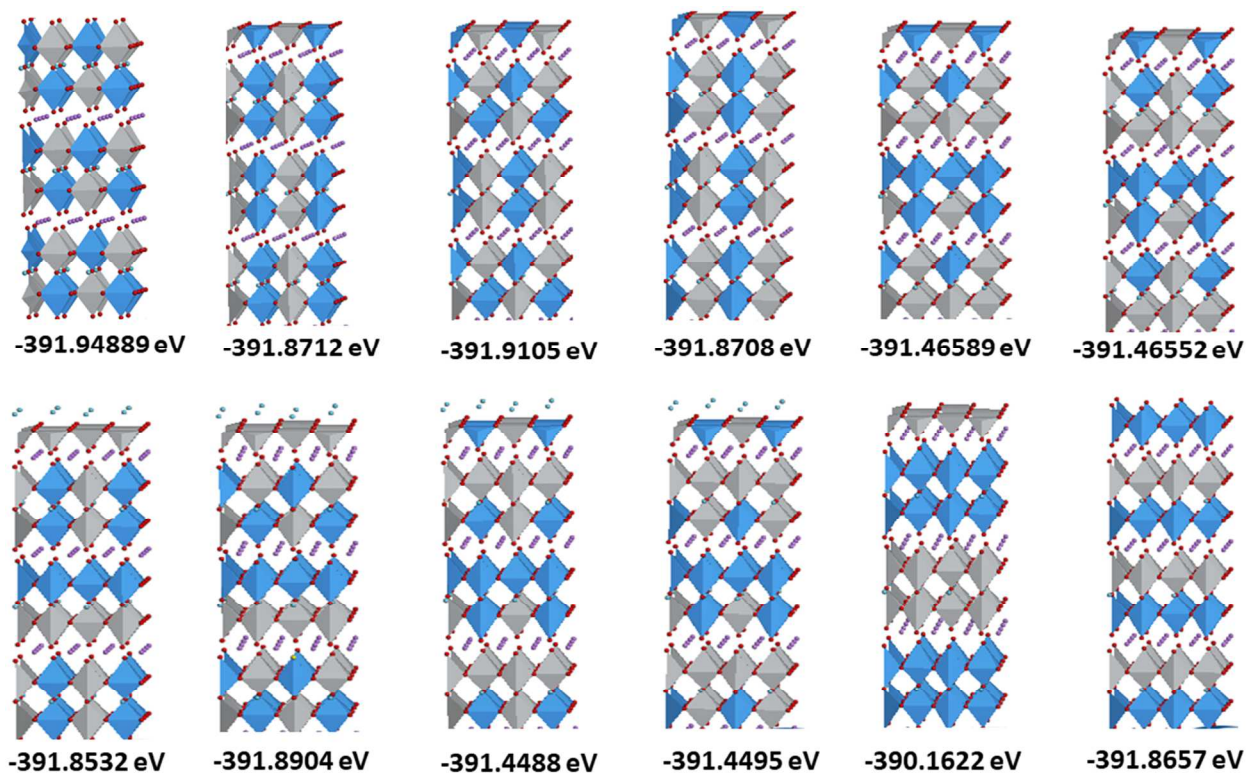-391.8532 eV   -391.8904 eV   -391.4488 eV   -391.4495 eV   -390.1622 eV   -391.8657 eV

Figure 10. DFT optimized structures for $Li_2La(TaTi)O_7$ and their corresponding total energy per unit cell. The top left configuration has the lowest energy. Gray and blue octahedra represent TaO_6 and TiO_6. Lithium atoms are shown as small spheres between the stacks.
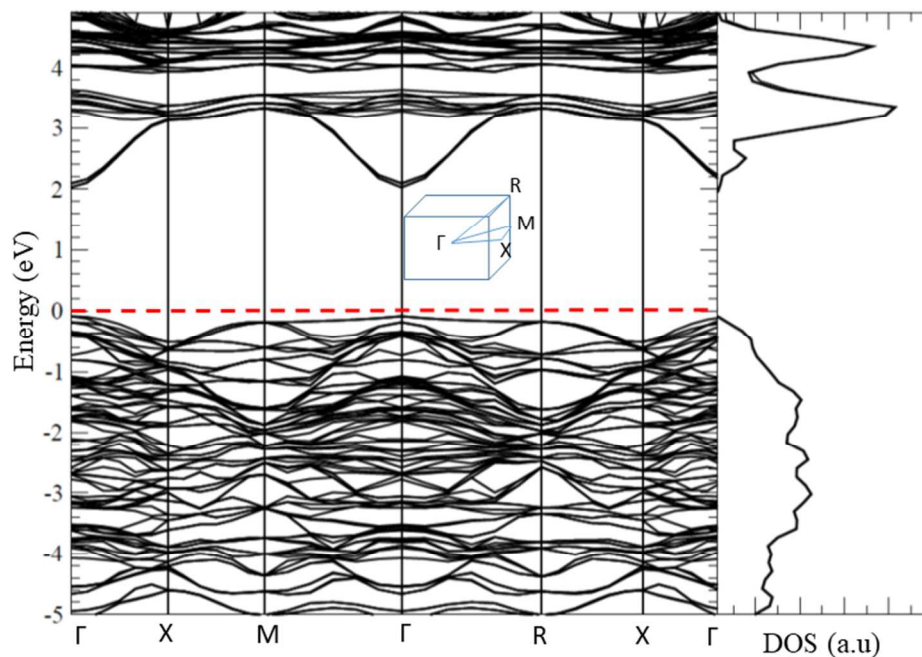
Figure 11. Calculated electronic band structure (right panel) and DOS (right panel) of the optimized $Li_2La(TaTi)O_7$ structure. The red dashed line indicates the fermi energy, and the insert is the Brillouin zone with special high symmetry k points.
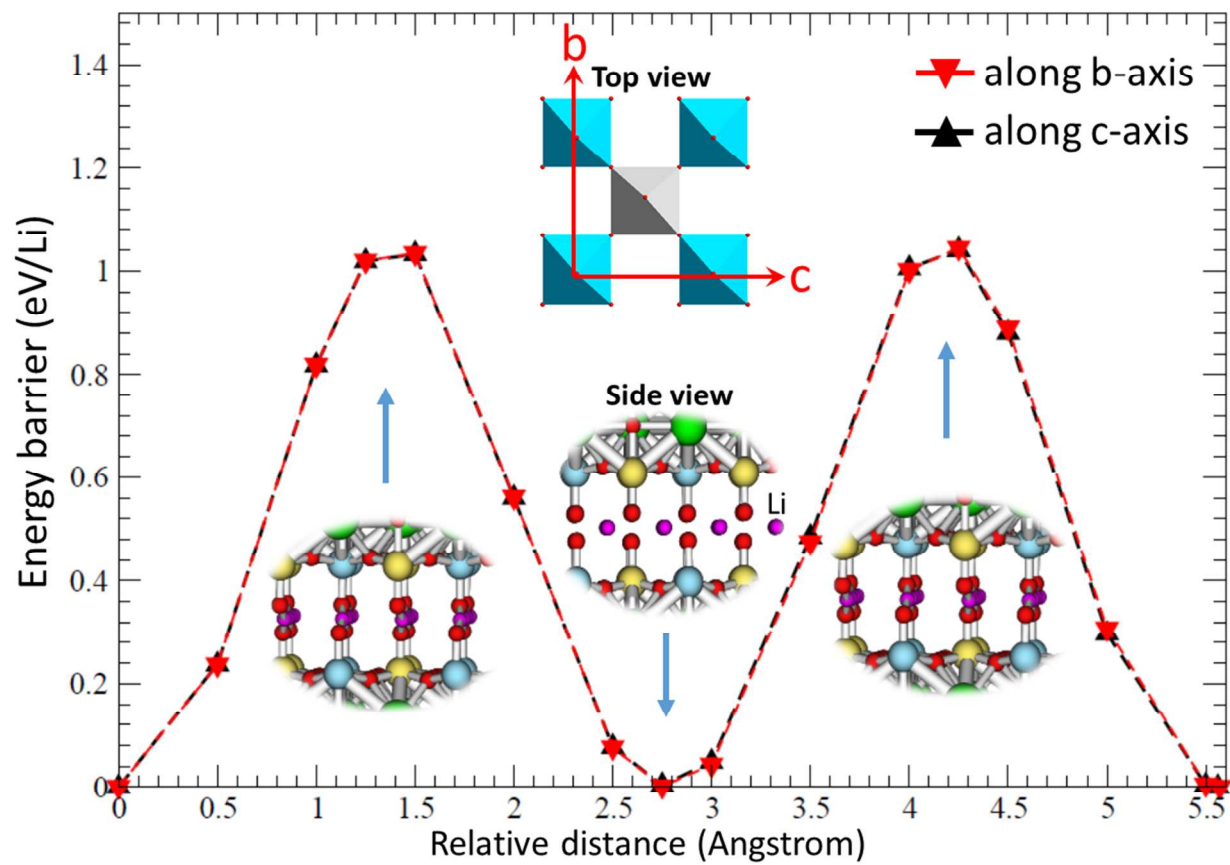
Figure 12. Energy barrier as a function of displacement of Li atoms from their original sites. The insets show the structures at maximum and minimum energy barriers.

Table 1. Refined structural parameters from Rietveld refinement with powder neutron diffraction data for $Li_2La(TaTi)O_7$. Space group *Cmcm*, $a = 18.2384(5)$, $b = 5.5126(2)$, $c = 5.4996(2)$ Å, Rp = 0.0440, wRp = 0.0185.

Atom	x	y	z	Occupancy	U_{iso}	Multiplicity
La1	0	0.2582(4)	0.25	1	0.0061(2)	4
Ta1	0.1164(2)	0.7543(9)	0.25	0.5	0.0002(3)	8
Ti1	0.1164(2)	0.7543(9)	0.25	0.5	0.0002(3)	8
Li1	0.2616(3)	0	0	1	0.0136(7)	8
O1	0	0.6994(4)	0.25	1	0.0102(5)	4
O2	0.21597(9)	0.7803(4)	0.25	1	0.0088(3)	8
O3	0.6112(1)	0	0	1	0.0099(3)	8
O4	0.09107(7)	0	0	1	0.0047(2)	8

Table 2. Refined structural parameters from Rietveld refinement with powder X-ray diffraction data for $Li_{1.8}La(Ta_{1.2}Ti_{0.8})O_7$. Space group: *I4/mmm*, $a = 3.8986(0)$Å, $c = 18.4520(3)$ Å, Rp= 0.0736, wRp = 0.0977

Atom	x	y	z	Occupancy	U_{iso}	Multiplicity
La	0	0	0	1	0.0214(7)	4
Ta1	0	0	0.38366(9)	0.6	0.0152(6)	8
Ti1	0	0	0.38366(9)	0.4	0.0152(6)	8
Li1	0	0.5	0.25	0.9	0.0250	8
O1	0	0.5	0.1063(5)	1	0.022(3)	4
O2	0	0	0.2872(7)	1	0.032(4)	8
O3	0	0	0.5	1	0.023(6)	8

Table 3: Variable temperature conductivity of $Li_2La(TaTi)O_7$ and $Li_{1.8}La(Ta_{1.2}Ti_{0.8})O_7$

Temperature (°C)	Total conductivity, σ (S cm^{-1})	
	$Li_2La(TaTi)O_7$	$Li_{1.8}La(Ta_{1.2}Ti_{0.8})O_7$
25	N/A	4.08611×10^{-9}
100	1.82184×10^{-8}	2.92588×10^{-7}
200	1.78362×10^{-7}	1.45776×10^{-5}
300	3.50991×10^{-6}	1.83973×10^{-4}
400	2.55058×10^{-5}	1.034851×10^{-3}

Table of contents entry